Cryo-EM structures of mouse bestrophin 1 channel in closed and partially open conformations

Kwon-Woo Kim^{1,†}, Euna Lee^{1,2,†}, Ara Ko^{1,2,†,‡}, Junmo Hwang¹, Kunwoong Park^{1,§}, Byoung-Cheol Lee¹, Ki Woo Kim³, Won-Jong Oh¹, Kyuhyung Kim², and Hyun-Ho Lim^{1,2,*}

¹Neurovascular Unit Research Group, Korea Brain Research Institute (KBRI), Daegu 41062, Republic of Korea, ²Department of Brain Sciences, DGIST, Daegu 42988, Republic of Korea, ³Division of Physiology, Department of Oral Biology, Yonsei University College of Dentistry, Seoul 03722, Republic of Korea

*Corresponding author. hhlim@kbri.re.kr https://doi.org/10.1016/j.mocell.2025.100208

ABSTRACT

Bestrophin 1 (BEST1) channels are calcium-activated CI⁻ channels involved in diverse physiological processes, including gliotransmitter release in astrocytes. Although human and chicken BEST1 orthologs have been extensively studied, the structural and functional properties of mouse BEST1 (mBEST1) remain poorly understood. In this study, we characterized the structure-function of mBEST1-BF, a C-terminally tagged variant, using whole-cell patch-clamp recordings, surface biotinylation assays, and single-particle cryo-electron microscopy. Cryo-electron microscopy structural analysis of mBEST1-BF revealed closed and partially open conformations. Comparative analysis with human and chicken BEST1 orthologs highlighted conserved calcium-binding and gating mechanisms, with distinct features in mBEST1, including a wider aperture sufficient to accommodate dehydrated CI⁻ ions and potential anion-binding sites near Val205 and GIn208 residues. The disordered C-terminal region of mBEST1 remains unresolved, suggesting it may require stabilizing factors for structural determination. Additionally, the autoinhibitory domain, which includes Ser354, likely plays a key role in regulating gating, with Ser354 potentially serving as a phosphorylation site that modulates channel activity. Our findings provide structural and functional insights into mBEST1 and suggest mechanisms underlying its unique gating and ion permeation properties.

© 2025 The Author(s). Published by Elsevier Inc. on behalf of Korean Society for Molecular and Cellular Biology. This is an open access article under the CC BY-NC-ND license (http://creativecommons.org/licenses/by-nc-nd/4.0/).

Keywords: Bestrophin 1, Calcium-activated chloride channel, Gating, Ion permeation, Structure-function

INTRODUCTION

Calcium-activated chloride channels play essential roles in various physiological processes, including ion homeostasis, epithelial transport, and cell volume regulation (Duran et al., 2010; Hartzell et al., 2005; Jentsch et al., 2002). Among these, the bestrophin (BEST) family of calcium-activated chloride channels has acquired significant attention due to its involvement in visual physiology and neuro-glial signaling of gliotransmission (Hartzell et al., 2008; Milenkovic et al., 2008; Oh and Lee, 2017). Bestrophin 1 (BEST1), the founding member of this family, was initially identified as the product of the *BEST1* gene, mutations in which are associated with Best vitelliform macular dystrophy, a hereditary retinal disorder (Bakall et al., 1999; Caldwell et al., 1999; Ponjavic et al., 1999). BEST1

However, while structural and functional studies have shed light on hBEST1 and chicken BEST1 (cBEST1) orthologs, the molecular mechanisms underlying mouse BEST1 (mBEST1) function remain poorly understood (Kane Dickson et al., 2014;

eISSN: 1016-8478 / © 2025 The Author(s). Published by Elsevier Inc. on behalf of Korean Society for Molecular and Cellular Biology. This is an open access article under the CC BY-NC-ND license (http://creativecommons.org/licenses/by-nc-nd/4.0/).

channels are highly conserved across species and exhibit diverse tissue-specific functions, with notable expression in the retina, brain, and other tissues (Bakall et al., 2003; Duta et al., 2004; Marmorstein et al., 2000). Human BEST1 (hBEST1) has been extensively studied in retinal pigment epithelium cells, where it mediates calcium-dependent chloride conductance critical for fluid transport and ion homeostasis (Hartzell et al., 2008; Sun et al., 2002). Beyond its retinal roles, BEST1 mouse ortholog has been suggested to be implicated in neuronal and astrocytic signaling, particularly in the release of gliotransmitters such as glutamate, GABA, and D-serine (Han et al., 2013; Jo et al., 2014; Koh et al., 2022; Lee et al., 2010; Oh et al., 2012; Woo et al., 2012). These findings highlight the importance of BEST1 as a key regulator of excitatory and inhibitory signaling pathways in the central nervous system.

[†] These authors equally contributed to this work.

^{*} Present address: National Cancer Center, Goyang-si, Gyeonggi-do 10408, Republic of Korea.

 $^{^{\}S}$ Present address: Baobab AiBIO Co, Ltd, Incheon 21984, Republic of Korea.

Miller et al., 2019; Owji et al., 2020, 2022a, 2022b; Vaisey and Long, 2018; Vaisey et al., 2016). Previous studies have demonstrated that mBEST1 mediates calcium-dependent anion currents in astrocytes and contributes to gliotransmitter release, suggesting its physiological importance in brain signaling (Han et al., 2013; Jo et al., 2014; Koh et al., 2022; Lee et al., 2010; O'Driscoll et al., 2009; Oh et al., 2012; Park et al., 2009; Woo et al., 2012). However, electrophysiological and structural characterization of mBEST1 in heterologous systems has proven challenging due to low protein expression and inconsistent functional measurements (Kim et al., 2023; O'Driscoll et al., 2009). Furthermore, the molecular basis of its gating, ion selectivity, and regulation remains unclear, particularly in comparison to its well-characterized orthologs. Recent structural studies have provided high-resolution structures of several BEST1 orthologs, revealing key insights into their gating mechanisms, anion conduction pathways, and conformational transitions between closed, partially open, and open states (Kane Dickson et al., 2014; Miller et al., 2019; Owji et al., 2022a; Pant et al., 2024; Vaisey et al., 2016; Wang et al., 2024). For example, structural studies of hBEST1 and cBEST1 have identified conserved calcium-binding sites (Ca2+-clasp), gating residues in the neck region, and anion-selectivity filter of the aperture. These structural features form the basis for calciumdependent gating and ion permeation. Despite these advances, mBEST1 exhibits unique functional and structural characteristics that distinguish it from its orthologs, such as its role in astrocytic signaling and gliotransmitter release. The lack of detailed structural and functional studies for mBEST1 limits our understanding of how these unique properties arise.

In this study, we aimed to address this gap by characterizing mBEST1 using a combination of electrophysiology, biochemistry, and structural biology. To overcome expression challenges, we engineered a C-terminally tagged mBEST1 construct (mBEST1-BF) and achieved robust protein expression in HEK293 GnTI⁻ cells. Using single-particle cryo-electron microscopy (cryo-EM), we resolved the closed and partially open conformations of mBEST1 at near-atomic resolution. Comparative structural analysis with hBEST1 and cBEST1 revealed conserved calcium-binding and gating mechanisms but also highlighted unique features of mBEST1, including its wider pore aperture and distinct C-terminal region. Additionally, we identified potential anion-binding sites in mBEST1 that may play roles in ion permeation and gating regulation. By integrating structural and functional data, our study provides new insights into the molecular mechanisms underlying mBEST1 gating and ion conduction. These findings contribute to a deeper understanding of BEST1 channels in general and pave the way for future investigations into their physiological roles in astrocytic signaling and brain function.

MATERIALS AND METHODS

Plasmid Construct, Cell Culture, and Transfection

The full coding sequence of mBEST1 (NM_011913.2) was cloned into the EEV vector (System Biosciences), with a 3C protease cleavage site fused in-frame to the BRIL-3xFLAG tag coding sequence at the 3'end. HEK293 GnTI⁻ cells were

cultured in a suspension system at 37°C under 5% humidified CO $_2$ with shaking at 150 rpm, using FreeStyle 293 Expression Medium (Thermo Fisher Scientific) supplemented with 2% ($v\!/v$) heat-inactivated fetal bovine serum (Thermo Fisher Scientific) and 0.05% ($v\!/v$) Poloxamer (Sigma-Aldrich). For transfection, the cell density was adjusted to 1.0 × 106/ml. The mBEST1-BRIL-3xFLAG (mBEST1-BF) construct was mixed with OPTI-MEM in a 1:20 ratio to the transfection volume and combined with a 1:6 DNA to polyethylenimine (PEI) transfection reagent ratio.

Whole-Cell Patch-Clamp Recording

Whole-cell patch-clamp recordings were performed on HEK293T cells transiently transfected with 1.0 µg of mBEST1-BF plasmid DNA and 0.2 µg of GFP plasmid DNA using PEI transfection reagent, following the manufacturer's instructions (Polysciences). Twenty-four hours post transfection, the cells polv-L-lysine-coated were plated onto alass chips. Electrophysiological recordings were conducted 30 to 48 hours post transfection. Patch pipettes were prepared from borosilicate glass capillaries (World Precision Instruments) using a P-1000 micropipette puller (Sutter Instruments) and fire-polished with an MF-900 microforge (Narishige) to achieve a pipette resistance of 3 to 5 M Ω . Recordings were performed on cells exhibiting green fluorescence, utilizing a MultiClamp 700B amplifier connected to an Axon Digidata 1550B digitizer (Molecular Devices). Signals were sampled at 10 kHz and lowpass filtered at 4 kHz with a 4-pole Bessel filter.

The bath solution contained 140 mM NaCl, 4 mM KCl, 2 mM $CaCl_2$, 10 mM HEPES, and 1 mM $MgCl_2$, adjusted to pH 7.3 with NaOH. The pipette solution consisted of 145 mM CsCl, 2 mM $MgCl_2$, 8 mM HEPES, and 5 mM EGTA, adjusted to pH 7.3 with CsOH. Free calcium concentrations were adjusted by adding $CaCl_2$, calculated using MaxChelator (https://somapp.ucdmc.ucdavis.edu/). Ionic currents of BEST1 channels were measured by applying 0.5-second voltage steps ranging from -100 mV to +100 mV in 20-mV increments, following a 0.1-second holding potential at 0 mV. Macroscopic channel events were analyzed using Clampfit 11.2 software (Molecular Devices) and Origin 9.1 software (OriginLab Corporation).

Surface Biotinylation

To evaluate the surface protein expression levels of BEST1 channels, surface biotinylation was performed (Roh et al., 2025). In HEK293T, cells (#CRL-3216, ATCC) were transiently transfected with mBest1 plasmid using PEI following the manufacturer's instructions. After the transfection, the cells were incubated for 48 hours under standard culture conditions. For surface biotinvlation, the cells were washed twice with ice-cold phosphate-buffered saline (PBS) and incubated on ice with 0.25 mg/ml EZ-Link Sulfo-NHS-SS-Biotin (#21331, Thermo Fisher Scientific) in PBS for 20 minutes. Unreacted biotin was removed by washing the cells with PBS, and cells were quenched using 50 mM glycine (pH 7.5) for 5 minutes. Cells were harvested and lyzed using a lysis buffer containing 1% Triton X-100 in PBS supplemented with a protease inhibitor cocktail. The lysates were clarified by centrifugation, and the supernatant was collected as whole-cell lysate. Biotinylated surface proteins were isolated from the lysates using NeutrAvidin Plus UltraLink resin (#53151, Thermo Fisher Scientific). The resin was extensively washed with lysis buffer to remove unbound proteins, and bound proteins were eluted using 2× LDS sample buffer. Total and surface protein samples were resolved by SDS-PAGE on a Bolt 4% to 12% Bis-Tris Plus Gel (Invitrogen) and transferred to a PVDF membrane using the iBlot 2 Transfer Stack system (Invitrogen). Immunoblotting was carried out using primary antibodies, including anti-HRV3C (#PA1-188, Invitrogen), antiactin (#8457S, Cell Signaling Technology), and antitransferrin receptor (#13-6800, Invitrogen). Membranes were developed with Clarity Western ECL substrate (Bio-Rad), and protein bands were visualized using the ChemiDOC Imaging System.

Protein Purification in Mammalian Cells

In all cases, purification procedures were conducted at 4°C or on ice unless stated otherwise. Protein purification of mBEST1-BF was initiated 48 hours after transfection. Transfected cells were harvested and resuspended in 50 ml of cell lysis buffer consisting of 50 mM Tris-HCl (pH 8.0), 300 mM NaCl, 1 mM phenylmethylsulfonyl fluoride, a spatula-tip amount of DNase I. and an EDTA-free protease inhibitor cocktail (Roche). Cell lysis was facilitated using a Dounce homogenizer. Subsequently, 2% (w/v) lauryl maltose neopentyl glycol (LMNG; Anatrace) detergent was added to the lysis buffer, and the proteins were extracted over ~2 hours. Following extraction, the mixture was centrifuged at 40,000 rpm for 40 minutes using an Optima XE-90 ultracentrifuge equipped with a Type 50.2 fixed-angle rotor (Beckman Coulter). The resulting clear supernatant was combined with pre-equilibrated FLAG resin (Thermo Fisher Scientific) in a buffer containing 300 mM NaCl, 50 mM Tris-HCl (pH 8.0), and 0.2 mM LMNG. The mixture was incubated for 1 hour to facilitate protein binding. The resin was washed thoroughly, and the bound proteins were eluted using 4 ml of FLAG peptide (Thermo Fisher Scientific). The eluate was concentrated using a 50-kDa cutoff concentrator (Amicon Ultra; MillporeSigma) at 4.000g for 10 to 15 minutes. Any sediment present in the protein solution was removed by centrifugation through a Spin-X filter (Corning Costar). The proteins were further purified using size-exclusion chromatography on a Superose-6 column (GE Healthcare) in a buffer containing 150 mM NaCl, 10 mM Tris-HCl (pH 8.0), and 0.05 mM LMNG. The purity of the resultant protein was assessed using FPLC chromatograms and SDS-PAGE.

Cryo-EM Data Collection and Image Processing

Single-particle cryo-EM for mBEST1-BRIL-3xFLAG was conducted in the presence of 5 μM free [Ca²+]. The 5 μM free [Ca²+] solution, buffered with 5 mM EGTA, was calculated using Maxchelator software. A Ca²+/EGTA solution was added to the protein solution to adjust free [Ca²+] at 5 μM and incubated for 1 minute prior to vitrification. For vitrification, 4 μl of protein samples were loaded onto glow-discharged carbon grids, maintained at 4°C, and 100% humidity. These grids were subsequently plunged into liquid ethane to vitrify the samples. The vitrification process was performed semiautomatically using a Vitrobot system (Thermo Fisher) at the Center for

Macromolecular and Cell Imaging, Seoul National University. Freshly vitrified protein grids were then transferred to a 200-kV Glacios cryo-EM, also located at the Center for Macromolecular and Cell Imaging, for single-particle imaging. The imaging conditions were as follows: applied defocus at $-2.00~\mu m$, dose rate of 40.57 e-/nm², exposure time of 6.90 seconds, image size of 4,096 \times 4,096 pixels, and a pixel size of 0.087 nm. The maximum, mean, and minimum intensity values were recorded as 13,954, 9,321.03, and 4,702, respectively.

When data acquisition was complete, movie files collected for mBEST1 were imported into CyroSPARC (v. 4.1.0) (Punjani et al., 2017). The particles were aligned using patch motion correction, followed by contrast transfer function (CTF) estimation through patch CTF. An initial protein template was generated via the automatic selection of small particles from 2,799 micrographs. These particles underwent multiple rounds of two-dimensional (2D) classification to eliminate poor-quality particles and refine the 2D template. As a result, 126,430 particles were selected from an initial total of 2,743,694 particles. To ensure an adequate number of particles. Topaz cross-validation was conducted for Topaz training, utilizing reference particles obtained from template picking. The particles were subsequently extracted through Topaz extraction. Particles from both template picking and Topaz picking were combined, and duplicates were removed. Multiple additional rounds of 2D classification were performed to eliminate false positives, ultimately yielding 366,146 particles. For three-dimensional (3D) reconstruction, an initial model was derived using ab initio reconstruction. Heterogeneous refinement was then employed to filter out poor-quality particles, resulting in the selection of 166,562 particles for the consensus map. Homogeneous refinement with C5 symmetry was applied, yielding a resolution of 2.95 Å. To identify distinct particle classes, 3D classification was performed, sorting the particles into 8 classes. These were further categorized into 2 primary groups: "alone" and "docked." The "docked" class exhibited variations in electron density near the Ile76 residues and was subdivided into "closed" and "partially open" conformations. Finally, nonuniform refinement was performed to generate the final maps for the "alone," "closed," and "partially open" classes (Punjani et al., 2020). The final maps achieved resolutions of 3.18, 3.18, and 3.10 Å for the "alone," "closed," and "partially open" classes, respectively. All maps were refined with C5 symmetry and optimized using per-particle defocus and per-group CTF parameters during refinement. Local resolution was assessed using the local resolution estimation tool implemented in cryoSPARC.

Model Building and Refinement

The initial model for mBEST1 was derived from the cBEST1 template (PDB 6N23). To construct the structural model of mBEST1, the cBEST1 structure was manually positioned within the EM density of mBEST1, and its 3D orientation was adjusted using UCSF Chimera 1.16. Subsequently, the mBEST1 structural model was manually built and refined using Coot software. The model generated in Coot was further refined using the real-space refinement tool within the Phenix program suite (Afonine et al., 2018). The pore diameter was calculated using HOLE program (Smart et al., 1996). The root-mean-square deviation

(RMSD) was calculated by using the open-source pymol script (https://github.com/tongalumina/rmsdca).

RESULTS

Expression and Electrophysiological Examination of mBEST1 Channel

We initially sought to express the mBEST1 channel in mammalian cell lines, including HEK293T and CHO-K1 cells. Both untagged full-length mBEST1 and tagged mBEST1 constructs (N-terminal 3X Flag and C-terminal 3X Flag fusions) exhibited minimal expression levels, as determined by western blot analysis. Additionally, their electrophysiological activity could not be detected via whole-cell patch-clamp recordings from transiently transfected HEK293T cells. These observations suggest that the low-level expression of mBEST1 may hinder its electrophysiological characterization. Interestingly, we discovered that the expression levels of mBEST1 could be significantly enhanced by adding a C-terminal tandem tag of BRIL and 3X Flag (mBEST1-BF) (Chun et al., 2012; Kim et al., 2023). Thus, we aimed to functionally characterize the mBEST1-BF channel using whole-cell patch-clamp recordings, comparing it to the human BEST1 (hBEST1-BF) channel bearing an identical C-terminal tag. While [Ca2+]i-dependent Cl currents were successfully recorded in hBEST1-BF-transfected cells, yielding an EC₅o value of ~170 nM and a Hill coefficient of ~3.4, no such currents were detected in mBEST1-BF-transfected HEK293 cells (Figs. 1A-C and S1).

To evaluate the protein expression and plasma membrane localization of mBEST1-BF and hBEST1-BF, we performed surface biotinylation assays, using β-actin and transferrin receptor as controls for total and membrane-specific protein, respectively (Fig. 1D). Surprisingly, the expression levels and surface localization of mBEST1-BF were comparable to those of hBEST1-BF. These findings prompted us to determine the structure of mBEST1 to better understand the functional discrepancies between the orthologs. Although key residues critical for calcium binding (Ca2+-clasp), gating (neck), and anion selectivity (aperture) are highly conserved among BEST1 orthologs, the poorly conserved and structurally unresolved Cterminal regions may play a significant role (Fig. S2) (Kim et al., 2023; Qu et al., 2007; Tsunenari et al., 2003). Notably, structurally determined regions in BEST channel homologs have been largely confined to the highly conserved N-terminal regions either due to the use of truncated proteins for structural determination (Kane Dickson et al., 2014; Miller et al., 2019; Owji et al., 2020, 2022b) or the inherently disordered nature of the C-terminal regions (Owji et al., 2022a).

Structural Determination of mBEST1 Channel

Recent structural studies on chicken, human, and bovine BEST channels have revealed multiple conformations corresponding to closed, partially open, and fully open states (Kane Dickson et al., 2014; Miller et al., 2019; Owji et al., 2020, 2021, 2022a, 2022b). To gain structural insights into the functional differences between mBEST1 and other BEST channel homologs, we expressed mBEST1-BF in HEK293 GnTI⁻ cells, solubilized it using LMNG detergent, and purified it for single-particle cryo-EM

imaging (Fig. S3). Purified proteins were incubated with 5 µM Ca²⁺ (EGTA-buffered) for 1 minute immediately before freezing. The structures were resolved at a resolution of 3.1 to 3.18 Å (Figs. 2 and 3, S3-S5, Table S1). 2D-averaged particle images revealed two distinct populations based on oligomeric states: pentamer and dimer-of-pentamer. The latter represented a bottom-to-bottom (cytoplasmic side-to-cytoplasmic side) assembly of 2 pentameric mBEST1 channels (Figs. 2 and S3). Three-dimensional structural classification showed that the particles in the pentameric state were in a closed conformation, whereas the docked particles exhibited 2 distinct conformations: closed and partially open. The structures of the "alone-closed" and "docked-closed" particles were essentially identical (RMSD = 0.16 Å) (Fig. 2B). Interestingly, an unknown density was detected between the docked cytoplasmic domains, although its molecular identity remains unclear (Fig. 2C).

Structural Comparison to the BEST1-Channel Orthologs: Permeation

The overall pentameric architectures of the "closed" and "partially open" conformations were very similar, with the primary difference observed at residue Ile76, which exhibited a Ca RMSD of ~5 Å between the 2 states (Fig. 3A and B) (Owji et al., 2022a). Similar to other BEST channel structures, mBEST1 contains 2 physical constrictions along the ion-conduction pore: the neck and the aperture (Fig. 3C-F). In the partially open conformation, the external pore mouth dilated due to the flipping back of Ile76, whereas Phe80 and Phe84 remained occluded (Figs. 3, S3, S6). The cytosolic aperture, formed by Val205 and Gln208 residues, maintained a radius of ~2.2 Å in both the closed and partially open conformations, sufficient to allow the permeation of dehydrated CI⁻ ions (Figs. 3D and F, S6). Structural comparisons with orthologs (hBEST1 in closed and partially open conformations, and cBEST1 in inactivated and open states) revealed that the aperture radii in the orthologs (hBEST1 closed ~0.9 Å; hBEST1 partially open ~1.7 Å; cBEST1 closed ~1.5 Å; cBEST1 open ~1.6 Å) were too narrow for CI permeation. In contrast, the aperture radius of the mBEST1 channel is sufficient to accommodate dehydrated Cl⁻ ions (Figs. 3C-F, S6).

Anion Binding in the mBEST1

Previous studies reported ion-like densities near the aperture region in a minor population (6.1% class) of Ca2+-bound hBEST1, where the Gln208 residues were oriented toward the center of the pore. Additionally, in hBEST2, the Lys208 residue was observed to coordinate an ion-like density near the aperture (Owji et al., 2022a). Interestingly, oval-shaped electron densities were identified near the Val205 residues in the aperture region of mBEST1, in both the C5 symmetry refined closed and partially open conformations (pink sphere, Fig. 4A). Given that the aperture radius of mBEST1 is wider than the radius of a dehydrated CI⁻ ion (~1.8 Å), these densities likely represent CI⁻ ions bound at the aperture, interacting with the Val205 residues. Further nonuniform refinement (C1 symmetry) revealed additional electron densities near the aperture, although these were located off the central pore axis. One of these densities was positioned close to the side chain of Gln208 (pink sphere,

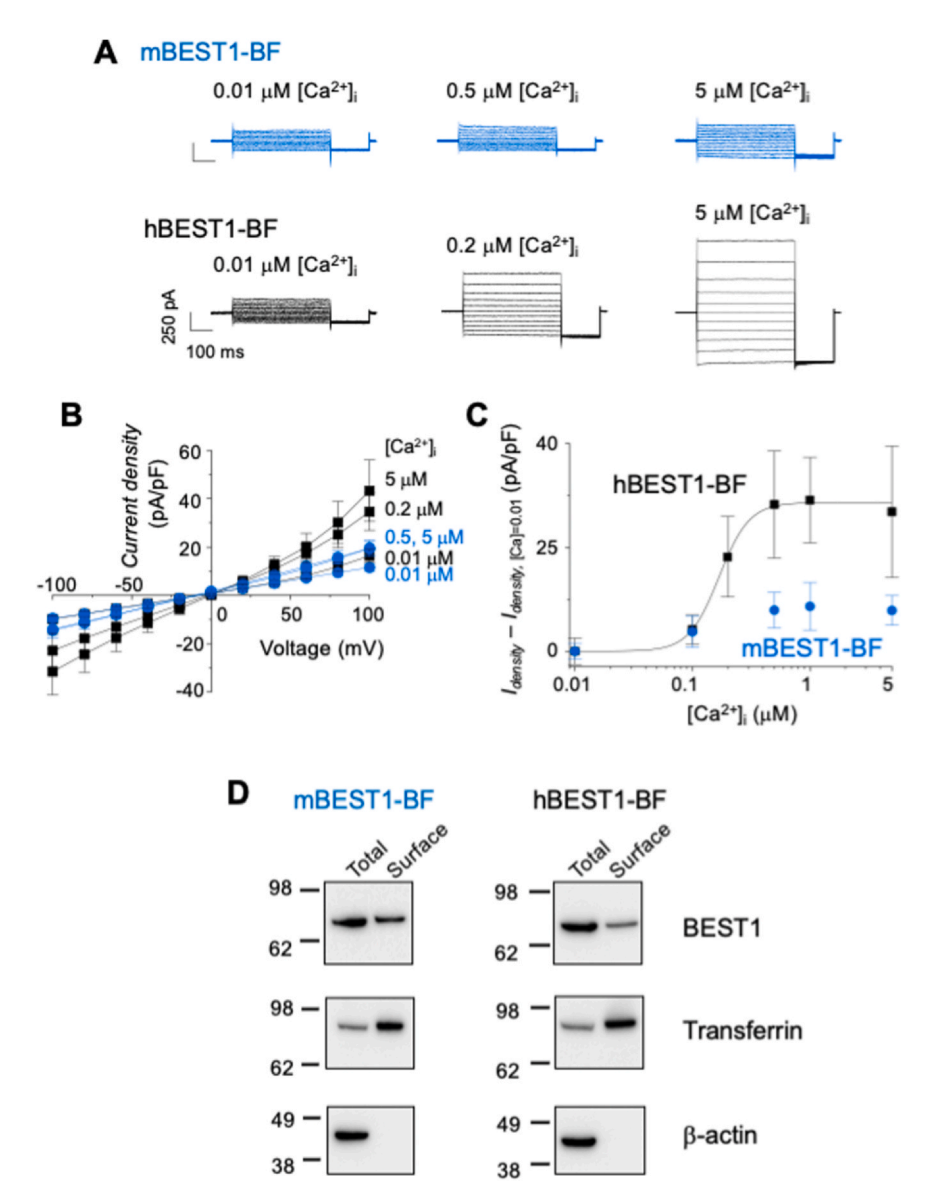


Fig. 1. Electrophysiological properties and surface expression of mBEST1 and hBEST1 channels. (A) Representative whole-cell current traces of mBEST1-BF (blue) and hBEST1-BF (black) recorded at the indicated $[Ca^{2+}]_i$. (B) Current-voltage (I-V) relationships of mBEST1-BF and hBEST1-BF, with current levels normalized to current densities. (C) Calcium-dependent activation of mBEST1-BF and hBEST1-BF at +100 mV. Current densities were calculated after subtracting baseline values at 0.01 μM $[Ca^{2+}]_i$. The number of observations at each $[Ca^{2+}]_i$ is as follows: for mBEST1-BF, 0.01 μM (n = 5), 0.1 μM (n = 6), 0.5 μM (n = 6), 1 μM (n = 6), and 5 μM (n = 8); for hBEST1-BF, 0.01 μM (n = 11), 0.1 μM (n = 12), 0.2 μM (n = 4), 0.5 μM (n = 17), 1 μM (n = 25), and 5 μM (n = 6). The calcium-dependent activation curve for hBEST1-BF was fitted using the Hill equation. (D) Total and surface expression of mBEST1-BF and hBEST1-BF were analyzed via western blotting. Anti-3C cleavage site antibodies were used to detect BEST1 proteins, while anti-β-actin and antitransferrin antibodies were used as loading controls for total protein and surface protein, respectively. The numbers and bars indicate molecular weights and locations of protein size markers, respectively.

Fig. 4B), while another extended from one of the Val205 residues (*red asterisk*, Fig. 4B). However, electron densities along the pore axis in C5 symmetry refined maps should be interpreted with caution, as they may result from symmetry enforcement during data processing rather than representing true features. Given the limitations of static cryo-EM snapshots in capturing ion occupancy and dynamics, further investigations are necessary to determine whether these densities correspond to bona fide CI⁻ binding sites.

Three CI⁻ binding sites were reported near the ion-conduction pore of cBEST1 channel (Kane Dickson et al., 2014). Prominent electron densities corresponding to 2 of these CI⁻ binding sites in cBEST1 were also observed in the mBEST1 structure (Fig. 4C). Site 1 is stabilized by the N-terminal helical dipole (S4a) and direct interactions with Tyr68, Tyr72, and Thr277 residues. These interactions are similar to those observed in the central CI⁻ binding site of CLC family proteins, where 2 N-terminal helical dipoles and the side chains of Tyr

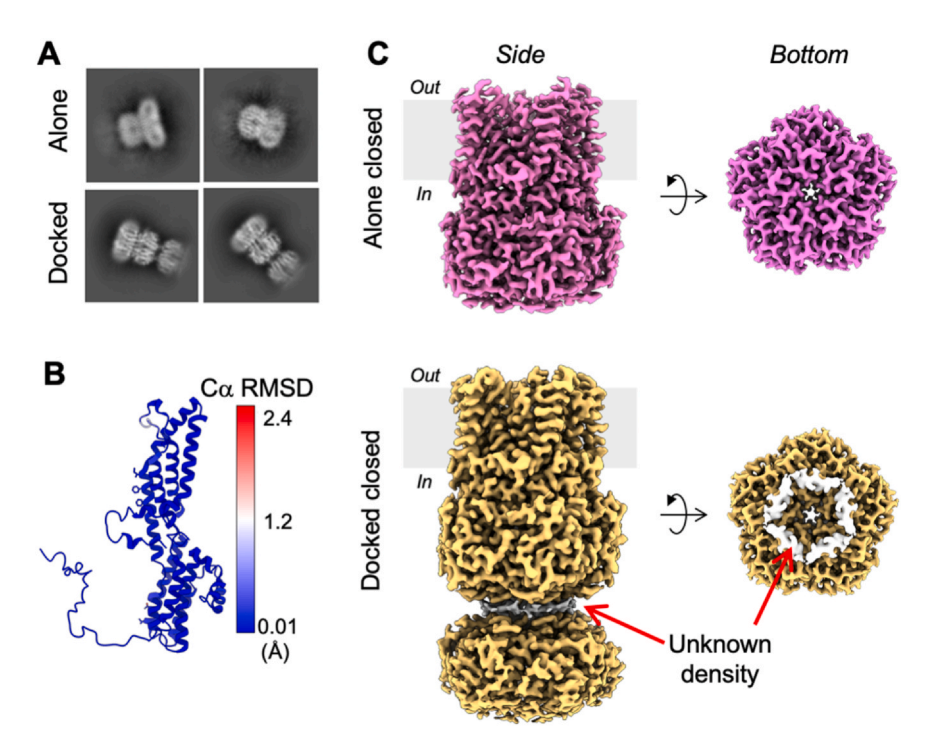


Fig. 2. Two distinct mBEST1 assemblies observed in EM images. (A) Representative 2D-averaged images of mBEST1 particles in 2 distinct assemblies: "alone" and "docked." (B) Cα RMSD comparison between the closed conformations of the "alone" and "docked" particles, showing structural similarity. (C) Electron density maps of the closed conformations for the "alone" and "docked" particles. Red arrows highlight an unidentified electron density (*white*) located between 2 docked mBEST1 channels.

and Ser residues coordinate CI⁻ binding (Dutzler et al., 2002; Park et al., 2019). Recent studies suggest that external GABA can also bind to Site 1. GABA binding induces a flipping of Ile76, rotation of the S2b helix, and opening of the neck region. Additionally, external treatment with GABA was shown to dose-dependently increase CI⁻ currents in both hBEST1 and cBEST1 (Pant et al., 2024; Wang et al., 2024). Site 2 provides another anion-binding site, supported by the N-terminal helical dipole (S2c), the side chain of Arg218 and T219, and the backbone amide of Arg105.

Structural Comparison to the BEST1-Channel Orthologs: Gating

Structural comparison of mBEST1 with hBEST1 and cBEST1 channels revealed a high degree of overall similarity, with notable variations concentrated near the external pore mouth region. This region is formed by the S1c helix-loop-S2a helix (residues 43-63) and the S3-S4 linker (residues 256-270) (Fig. 5A and B). In mBEST1, this region exhibited a slight rigidbody extension; however, the interaction networks within the external pore mouth remained largely unchanged (Figs. 5B, S7A). However, structural differences in the external pore mouth region have to be considered cautiously. Since it exhibits lower local resolution across different conformational states compared with other regions (Fig. S4), suggesting that the observed structural variations may primarily reflect intrinsic flexibility rather than functionally relevant differences. Notably, mBEST1 displayed prominent electron density in the calciumclasp region, similar to human and chicken orthologs,

supporting the hypothesis that it represents a Ca²⁺-bound inactivated state (Fig. 5C, *orange* boxes).

Although the full-length mBEST1 channel with BRIL and 3X Flag tags was used for structural determination, the C-terminal region of mBEST1 was disordered beyond lle366 (Fig. 5C, green boxes). A similar observation was made in the hBEST1 structure, where the C-terminal region was resolved only up to Pro377 (Owji et al., 2022a). These findings suggest that the C-terminal region of the BEST1 channel is inherently disordered and may require additional stabilizing factor(s) to visualize its structure fully. Consistently, the C-terminal region beyond residues 367 and 364 in the x-ray crystallographic and cryo-EM structures, respectively, of the C-terminal truncated cBEST1 (residues 1-405) also appeared disordered (Kane Dickson et al., 2014; Miller et al., 2019) (Fig. S7B and C).

As observed in cBEST1 and hBEST1 structures, the C-terminal region of mBEST1 wraps around the cytosolic portions of adjacent subunits (Fig. 5C, green boxes; Fig. S7B and C). Previous studies have suggested that the C-terminal sequence motif, referred to as the "autoinhibitory domain" (residues 356-364 in mBEST3 and hBEST3), "inactivation peptide" (residues 356-362 in cBEST1), and "Anchor" (residues 356-367 in hBEST1 and 357-368 in hBEST2), induces the inactivation of BEST channel activities (Owji et al., 2022a; Qu et al., 2006, 2007; Vaisey and Long, 2018; Xiao et al., 2008). The structural mechanisms underlying the binding and detachment of the autoinhibitory domain, which facilitate channel gating transitions (activation and inactivation), have been well-illustrated in the structures of hBEST1 (closed and partially open conformations)

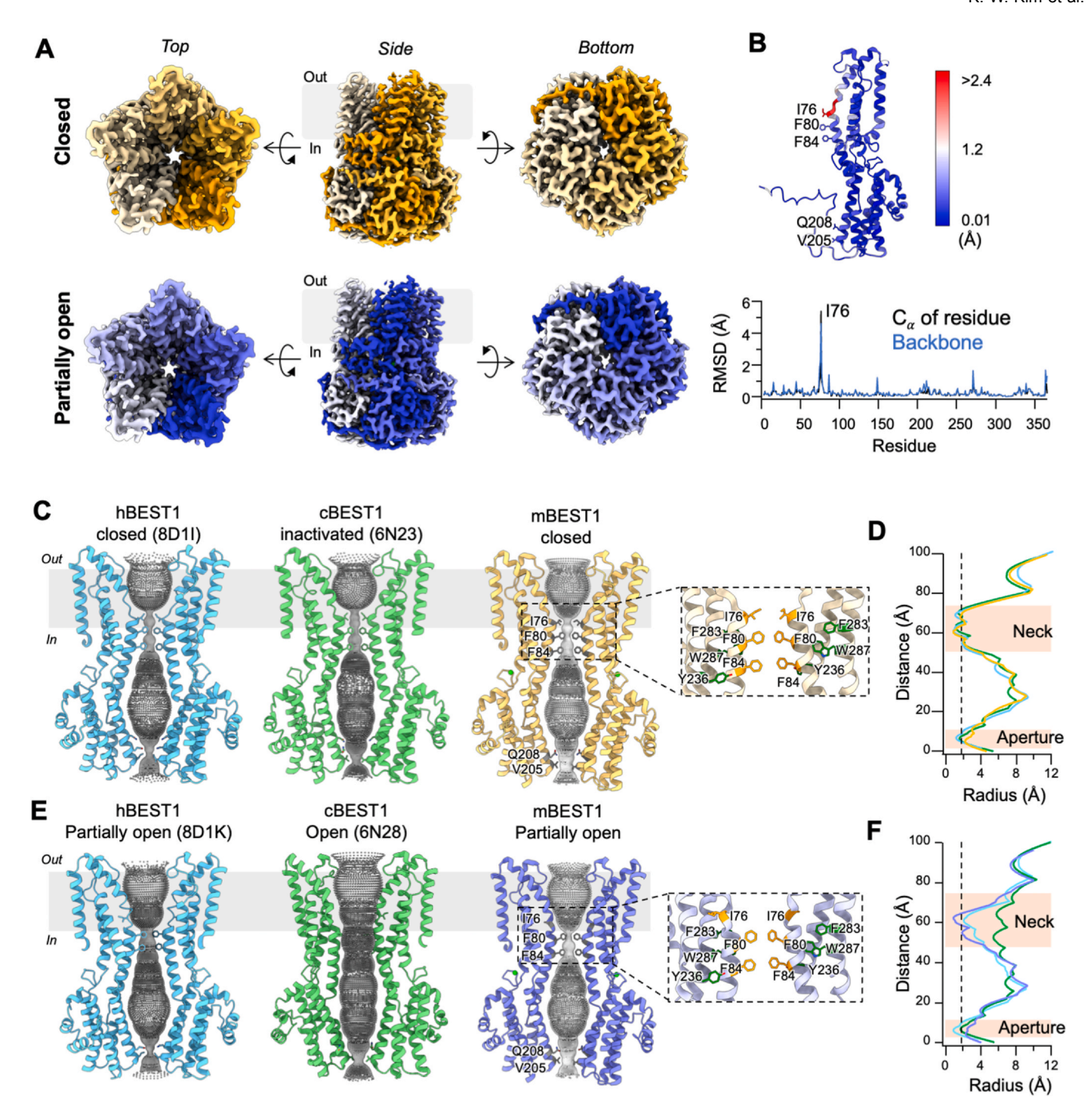


Fig. 3. Cryo-EM structures of the mBEST1 channel. (A) Electron density maps of mBEST1 in closed and partially open conformations (top, side, and bottom views). (B) RMSD analysis between the closed and partially open conformations. The top panel illustrates a cartoon representation of the analysis, while the bottom panel shows residue-by-residue Cα-RMSD and backbone-RMSD plots. (C-F) Ion-conduction pathways in BEST1-channel orthologs. (C) Closed (or inactivated) state structures of mBEST1, hBEST1, and cBEST1. (E) Partially open conformations of mBEST1 and hBEST1, along with the fully open conformation of cBEST1. For clarity, only 2 subunits are shown for each structure. Gray dots represent pore radii along the ion-conduction pathway, and dashed boxes highlight the neck region and conformational changes of Ile76 in mBEST1 structures. (D and F) Pore dimension plots derived from hole analysis corresponding to the structures in panels C and E, respectively. The colored lines indicate the pore radii of the BEST1 orthologs: hBEST1 (cyan), cBEST1 (green), mBEST1 closed conformation (yellow), and mBEST1 partially open conformation (purple-blue). The dashed lines represent the dehydration radius of Cl⁻ (~1.8 Å).

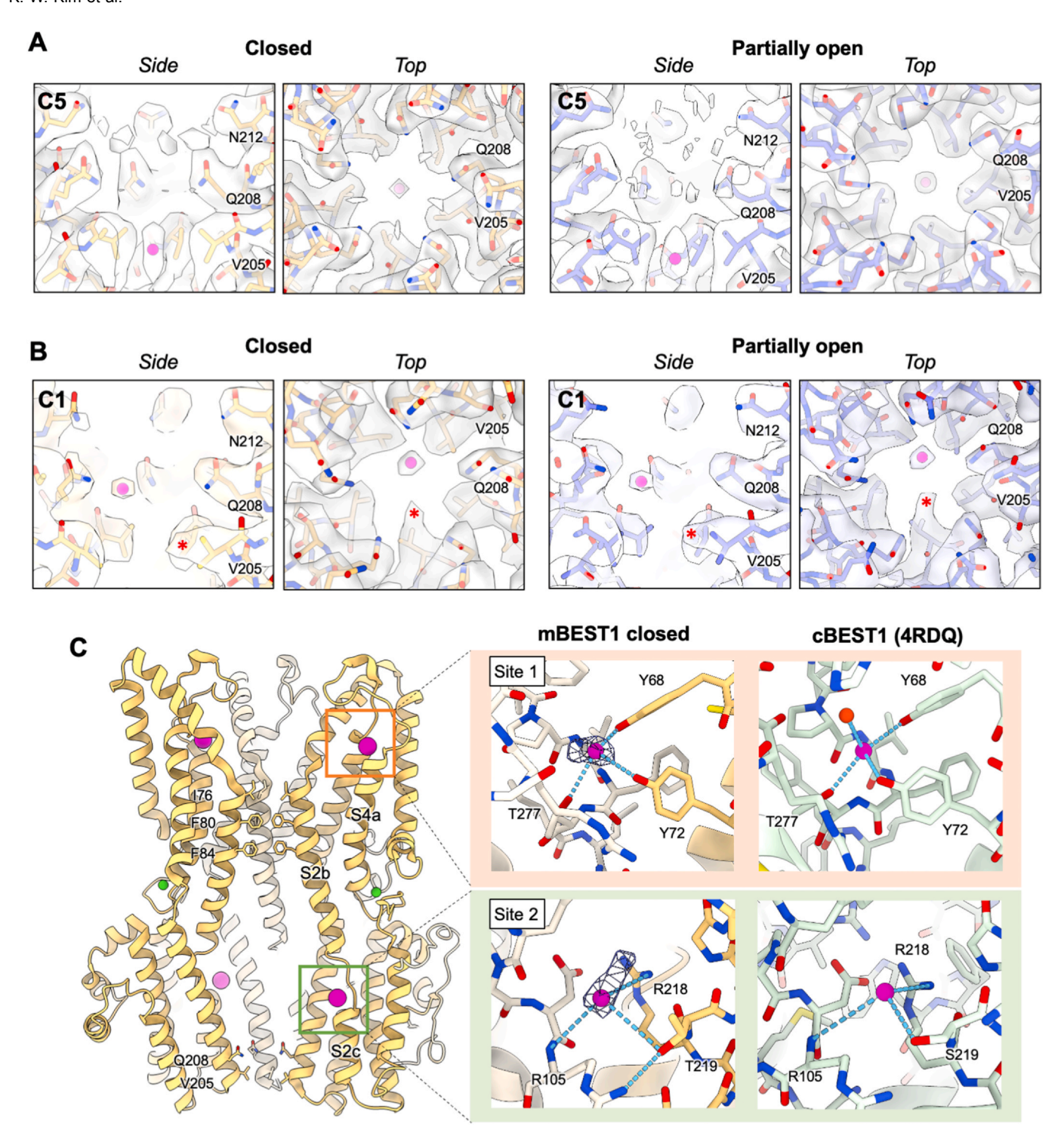
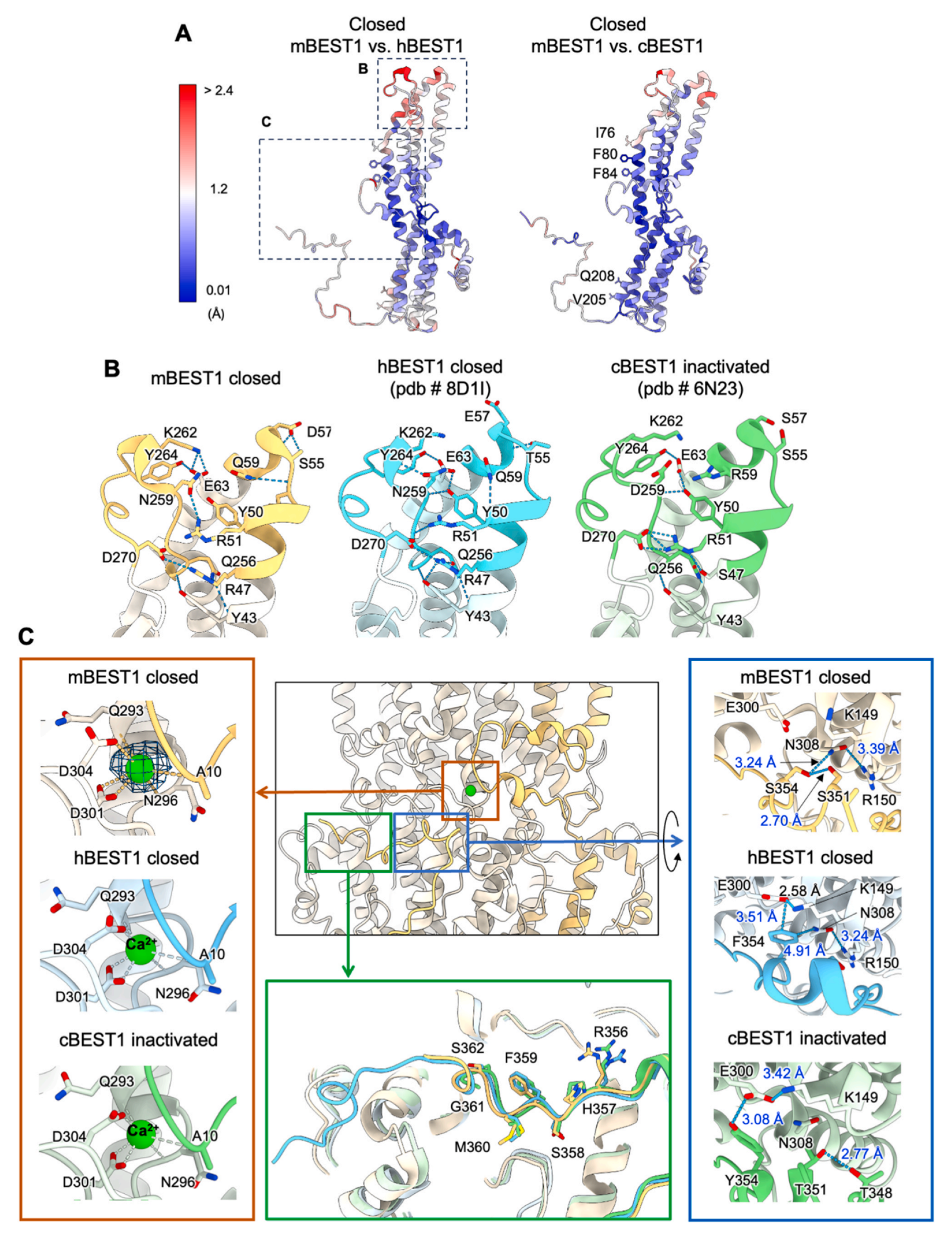


Fig. 4. Anion binding in mBEST1. (A and B) Electron density maps showing anion binding near the aperture region in mBEST1. (A) C5 symmetry refined map with *pink* spheres indicating "ion-like" density near the Val205 residue. (B) C1 nonuniform refined map, where *pink* spheres indicate density near the Gln208 residue, and the *red* asterisk highlights an extended density originating from Val205. (C) Cl binding sites in the pore mouth and cavity of mBEST1, with Cl ions depicted as *pink* spheres. The anion-coordination geometry in mBEST1 is compared with cBEST1 (PDB ID: 4RDQ), illustrating structural conservation and differences between the 2 channels.

and hBEST2 (closed and fully open conformations). In the hBEST1 structure, the Phe354 residue interacts directly with Asp300 and Asn304 residues, strengthening the attachment of the autoinhibitory domain to the channel periphery. However,

this interaction is disrupted in hBEST2 due to the non-conservation of Phe354 (Owji et al., 2022a). In mBEST1, we observed that the corresponding sequence motif for the "auto-inhibitory domain" ($_{356}$ RHSFMGS $_{362}$) binds to an adjacent



(caption on next page)

Fig. 5. Structural comparison among the BEST1 orthologs. (A) Cα-RMSD analysis comparing mBEST1 with hBEST1 and cBEST1 in their closed conformations. *Dashed* boxes highlight regions examined in detail in panels B and C. (B) Structural comparison of the external pore mouth region among mBEST1 (*yellow* cartoon), hBEST1 (*cyan* cartoon, PDB ID: 8D1I), and cBEST1 (*green* cartoon, PDB ID: 6N23). (C) Structural comparison of the channel periphery among the orthologs, with the same color representations as in panel B. Prominent electron density was observed in the calcium-binding site (Ca²+-clasp) of mBEST1 (*orange* boxes). Regions near the "autoinhibitory domain" are highlighted in *green* boxes, while residue-residue interaction networks involving S354 (mBEST1), F354 (hBEST1), and Y354 (cBEST1) are depicted in *blue* boxes.

subunit, which suggests that the mBEST1 structure may also represent an inactivated state (Fig. 5C, green boxes; Fig. S7B). A previous study showed that a phospho-mimic mutation of Ser358 (S358E) in cBEST1 eliminated inactivation by creating a physical clash between the autoinhibitory domain and the channel periphery, leading to detachment of the inactivation peptide from the adjacent subunit (Vaisey and Long, 2018). Interestingly, in mBEST1, Ser354 forms a hydrogen bonding network with Glu300, Asn308, and Ser351, potentially stabilizing the interaction between the autoinhibitory domain and the channel periphery, akin to the role of Phe354 in hBEST1 (Fig. 5C, blue boxes).

DISCUSSION

In this study, we provide structural and functional insights into the mBEST1 channel. Despite robust protein expression and proper plasma membrane localization of mBEST1-BF in HEK293T cells, calcium-dependent Cl⁻ currents were not detected. Structural analysis by cryo-EM revealed distinct closed and partially open conformations, along with specific structural features that may underlie its functional properties and gating mechanisms.

Functional Implications

The absence of CI⁻ currents in mBEST1-BF-transfected HEK293T cells, despite robust protein expression, proper plasma membrane localization in HEK293T cells, and its structural conservation with other BEST1 orthologs, suggests that mBEST1 functionality may depend on factors absent in this cellular system. These findings suggest several possibilities. First, the mBEST1 protein may produce an intrinsically inactive channel. However, previous studies demonstrated calcium-dependent CI⁻ currents for mBEST1 expressed in TREX-293 cells (fused with a C-terminal c-myc tag) or HEK293T cells (untagged mBEST1) (O'Driscoll et al., 2009; Park et al., 2009). Furthermore, mBEST1 has been implicated in calcium-dependent gliotransmitter releases, including glutamate, GABA, and Dserine in mouse brain astrocytes (Han et al., 2013; Koh et al., 2022; Lee et al., 2010; Park et al., 2015). Thus, it is unlikely that mBEST1 is inherently nonfunctional as an ion channel. This implies that specialized cellular components or post-translational modifications may be critical for its activation. One important future direction is to examine mBEST1 activity in its native cellular environment, such as mouse astrocytes, or in the heterologous cell system originated from mouse to identify specific cellular factors or post-translational modifications essential for its activation. These studies could shed light on why mBEST1 remains functionally inactive in HEK293T cells. Furthermore, understanding how mBEST1 contributes to astrocytic gliotransmitter release and its regulation by calcium signaling could reveal broader physiological implications of this channel. By addressing these questions, future studies can build upon our findings to enhance the understanding of mBEST1's unique structure and function.

A Dimer-of-Pentameric Assembly of mBEST1 Channel: Structural and Functional Implications

Cryo-EM analysis of mBEST1 revealed 2 distinct oligomeric states: a canonical pentameric form and an unexpected dimerof-pentamer assembly. While pentameric organization is a well-established feature of BEST channels, the observed bottom-to-bottom (cytoplasmic side-to-cytoplasmic side) dimerization raises intriguing questions regarding its structural basis, functional implications, and physiological relevance.

The dimer-of-pentameric assembly was observed in a subset of particles within our dataset and was classified as a distinct structural population. This arrangement suggests a potential interpentameric interface that may involve specific protein-protein interactions mediated by cytoplasmic elements. Given that BEST channels are not known to form higher-order oligomers under physiological conditions, the molecular dedriving dimerization remain terminants this Interestingly, we observed an unidentified density between the docked cytoplasmic domains, which may represent part of the flexible cytosolic C-terminal region contributing to interpentameric assembly formation. Additionally, the presence of a dimeric state could be influenced by the biochemical environment used for sample preparation. The use of LMNG detergent during solubilization and purification may have altered intersubunit interactions, stabilizing the dimeric form. If this dimer-ofpentameric organization is physiologically relevant, it could have significant consequences for BEST1-channel function. This structural arrangement may influence the cooperative gating of each pentamer, which is modulated by intracellular calcium and extracellular/luminal GABA (Pant et al., 2024; Wang et al., 2024), as well as impact ion-conduction properties between adjacent pentamers. Additionally, dimerization might serve a regulatory function in response to intracellular factors such as lipid composition, membrane tension, or interacting proteins. However, in our study, the absence of electrophysiological evidence for cooperative gating between pentamers suggests that the dimer-of-pentamer form may not be functionally active in a heterologous expression system.

To date, no dimer-of-pentameric state has been reported for the structures of other BEST homologs, including chicken, bovine, and hBEST1 and BEST2 channels, which remain exclusively pentameric (Kane Dickson et al., 2014; Miller et al., 2019; Owji et al., 2022a; Pant et al., 2024; Vaisey et al., 2016; Wang et al., 2024). This raises the possibility that the observed

dimerization is either a species-specific feature of mBEST1 or an artifact of sample preparation. However, similar higher-order oligomeric assemblies have been documented in other membrane proteins, particularly those involved in intercellular communication.

One comparable system is gap junction channels, where connexin hemichannels dock across adjacent membranes to facilitate direct intercellular communication (Kumar and Gilula, 1996). Also, the dimer-of-pentameric assembly of mBEST1 shares conceptual similarities with Aquaporin-0 (AQP0) membrane junctions, where AQP0 tetramers in adjacent membranes form intercellular junctions, effectively sealing off the water pore (Gonen et al., 2004). While both AQP0-mediated junctions and gap junctions involve intercellular interactions between extracellular domains, the interface between 2 pentamers of mBEST1 is the cytoplasmic domain. Thus, if a pentameric BEST1 channel is expressed in the plasma membrane, while another pentameric BEST1 channel is localized in an intracellular organelle membrane (eg, ER, endosome, or lysosome), these 2 could assemble into a bottom-to-bottom dimerof-pentameric structure, forming a continuous ion-conduction pathway from the organellar lumen to the extracellular space.

If biologically relevant, the dimer-of-pentameric BEST1 channel could provide a direct ion flux pathway between the extracellular space and the organelle interior. When both channels are open simultaneously, permeant ions could flow directly from the extracellular space into the organelle lumen or vice versa. This system could function analogously to gap junction channels, but instead of connecting 2 cells, it would connect 2 cellular compartments, potentially influencing endosomal trafficking and maturation via pH and ion balance modulation, lysosome-mediated degradation through Cl-dependent enzymatic activity, ER-plasma membrane crosstalk impacting calcium signaling, etc. Thus, it could be a potential dual-membrane signal relay system without alteration of membrane potential of cell membrane. Such a mechanism could enable a dual-membrane signal relay system, facilitating intracellular communication without altering the plasma membrane potential. On the other hand, if this BEST1-mediated bridging between the plasma membrane and an intracellular organelle membrane is dysregulated, it could create an uncontrolled ion-conduction pathway, leading to disruptions in organelle ion homeostasis, cellular signaling, and disease pathogenesis.

While the biological significance of this higher-order oligomer remains uncertain, its potential impact on channel function, regulation, and membrane organization warrants further investigation. Future studies combining structural, biochemical, and functional approaches will be essential to elucidate the relevance of this assembly in the broader context of BEST channel physiology.

Comparison With Orthologs: Ion Permeation and Gating

Structural comparisons highlight both conserved and distinct features of mBEST1 relative to hBEST1 and cBEST1. Notably, the aperture radius in mBEST1 is sufficient to accommodate dehydrated CI⁻ ions, unlike the narrower apertures of hBEST1 and cBEST1 in their closed, partially open, and fully open

conformations. The observed electron densities near Val205 and Gln208 further suggest potential Cl binding sites, which might contribute to ion selectivity. These findings suggest that while mBEST1 shares structural motifs with its orthologs, subtle differences in gating and permeation mechanisms may account for its unique functional properties.

The presence of 2 anion-binding sites in mBEST1 suggests their potential roles in modulating channel function. Site 1, given its location near gating-critical residues, may act as a regulatory site, linking anion binding to conformational transitions that influence channel opening. This aligns with findings in other BEST1 orthologs, where GABA binding to similar sites facilitates pore gating. In contrast, Site 2, positioned toward the cytoplasmic side of the pore, may play a complementary role. potentially influencing ion selectivity or stabilizing anion conduction pathways. Together, these sites could integrate anion binding with structural dynamics to finely regulate channel activity under physiological conditions.

The role of the C-terminal "autoinhibitory domain" in mBEST1 is supported by its similarity to other BEST1 orthologs. Our findings suggest that this domain interacts with adjacent subunits to stabilize the inactivated state, consistent with prior studies on cBEST1 and hBEST1. Interestingly, Ser354 in mBEST1 appears to form stabilizing interactions with surrounding residues, similar to the role of Phe354 in hBEST1. This raises the intriguing possibility that Ser354 phosphorylation could regulate mBEST1 gating, providing a testable hypothesis for future studies. Resolving the disordered C-terminal region of mBEST1 represents another critical challenge in the future. Experimental approaches that stabilize this region-for example, the use of cofactors or alternative sample preparation methods—could elucidate its structural and functional roles, including its potential involvement in gating regulation.

AUTHOR CONTRIBUTIONS

Kwon-Woo Kim: Writing – original draft, Investigation, Formal analysis. Ara Ko: Writing - original draft, Investigation, Formal analysis. Euna Lee: Writing - original draft, Investigation, Formal analysis. Kunwoong Park: Methodology. Junmo Hwang: Methodology. Ki Woo Kim: Writing - review & editing. Resources. Byoung-Cheol Lee: Writing - review & editing, Resources. Kyuhyung Kim: Writing - review & editing, Resources. Won-Jong Oh: Writing - review & editing, Resources. Hyun-Ho Lim: Writing – review & editing, Writing – draft. Supervision, Funding acquisition, Conceptualization.

DECLARATION OF COMPETING INTERESTS

We declare we have no competing interests.

DECLARATION OF GENERATIVE AI AND AI-ASSISTED TECHNOLOGIES IN THE WRITING PROCESS

During the preparation of this work, the author(s) used ChatGPT in order to check for the grammatical errors. After using this tool/service, the author(s) reviewed and edited the content as needed and take(s) full responsibility for the content of the publication.

ACKNOWLEDGMENTS

The authors thank Global Science experimental Data hub Center (GSDC) at Korea Institute of Science and Technology Information (KISTI) for computing resources and technical support. Use of cryo-EM facilities of NEXUS consortium under the project #NEXUS-2024-03-019 (to H.H. Lim) was supported by a National Research Foundation of Korea grant RS-2024-00440289. This work was supported by the Basic Science Research Program through the National Research Foundation of Korea (NRF) grants (2021R1A2C1004884 to H.H. Lim; 2022R1F1A1071221 to B.C. Lee), the Brain Research Program of the NRF (2020M3E5D9079766 to W.J. Oh) funded by the Ministry of Science and ICT, Republic of Korea, and the KBRI basic research program through Korea Brain Research Institute funded by the Ministry of Science and ICT (25-BR-01-02 and 25-BR-05-07 to H.H. Lim), the DGIST International Joint Research Project (24-KUJoint-07 to K.H. Kim), and the Korea Drug Development Fund funded by the Ministry of Science and ICT, the Ministry of Trade, Industry, and Energy, and the Ministry of Health and Welfare (HN22C0645 to K.W. Kim). We are grateful to the Lim lab members for their timely help throughout the work.

ORCID

Kwon-Woo Kim https://orcid.org/0000-0003-0449-2172
Euna Lee https://orcid.org/0009-0009-4985-4094
Ara Ko https://orcid.org/0009-0006-2032-678X
Junmo Hwang https://orcid.org/0000-0002-1398-5369
Kunwoong Park https://orcid.org/0000-0002-5666-8486
Byoung-Cheol Lee https://orcid.org/0009-0002-1635-9627
Ki Woo Kim https://orcid.org/0000-0002-7790-1515
Won-Jong Oh https://orcid.org/0000-0001-8867-7814
Kyuhyung Kim https://orcid.org/0000-0002-9943-5092
Hyun-Ho Lim https://orcid.org/0000-0002-5477-5640

APPENDIX A. SUPPLEMENTAL MATERIAL

Supplemental material associated with this article can be found online at: doi:10.1016/j.mocell.2025.100208.

Received December 8, 2024 Revised February 26, 2025 Accepted February 26, 2025 Available online 3 March 2025.

REFERENCES

Afonine, P.V., Poon, B.K., Read, R.J., Sobolev, O.V., Terwilliger, T.C., Urzhumtsev, A., and Adams, P.D. (2018). Real-space refinement in PHENIX for cryo-EM and crystallography. Acta Crystallogr. D Struct. Biol. 74, 531-544.

Bakall, B., Marknell, T., Ingvast, S., Koisti, M.J., Sandgren, O., Li, W., Bergen, A.A., Andreasson, S., Rosenberg, T., Petrukhin, K., et al. (1999). The mutation spectrum of the bestrophin protein–functional implications. Hum. Genet. *104*, 383-389.

Bakall, B., Marmorstein, L.Y., Hoppe, G., Peachey, N.S., Wadelius, C., and Marmorstein, A.D. (2003). Expression and localization of bestrophin during normal mouse development. Invest. Ophthalmol. Vis. Sci. 44, 3622-3628.

Caldwell, G.M., Kakuk, L.E., Griesinger, I.B., Simpson, S.A., Nowak, N.J., Small, K.W., Maumenee, I.H., Rosenfeld, P.J., Sieving, P.A., Shows, T.B., et al. (1999). Bestrophin gene mutations in patients with Best vitelliform macular dystrophy. Genomics, *58*, 98-101.

Chun, E., Thompson, A.A., Liu, W., Roth, C.B., Griffith, M.T., Katritch, V., Kunken, J., Xu, F., Cherezov, V., Hanson, M.A., et al. (2012). Fusion partner toolchest for the stabilization and crystallization of G protein-coupled receptors. Structure, *20*, 967-976.

Duran, C., Thompson, C.H., Xiao, Q., and Hartzell, H.C. (2010). Chloride channels: often enigmatic, rarely predictable. Annu. Rev. Physiol. 72, 95-121.

Duta, V., Szkotak, A.J., Nahirney, D., and Duszyk, M. (2004). The role of bestrophin in airway epithelial ion transport. FEBS Lett. *577*, 551-554.

Dutzler, R., Campbell, E.B., Cadene, M., Chait, B.T., and MacKinnon, R. (2002). X-ray structure of a CIC chloride channel at 3.0 A reveals the molecular basis of anion selectivity. Nature, *415*, 287-294.

Gonen, T., Sliz, P., Kistler, J., Cheng, Y., and Walz, T. (2004). Aquaporin-0 membrane junctions reveal the structure of a closed water pore. Nature, *429*, 193-197.

Han, K.S., Woo, J., Park, H., Yoon, B.J., Choi, S., and Lee, C.J. (2013). Channel-mediated astrocytic glutamate release via Bestrophin-1 targets synaptic NMDARs. Mol. Brain, *6*, 4.

Hartzell, C., Putzier, I., and Arreola, J. (2005). Calcium-activated chloride channels. Annu. Rev. Physiol. *67*, 719-758.

Hartzell, H.C., Qu, Z., Yu, K., Xiao, Q., and Chien, L.T. (2008). Molecular physiology of bestrophins: multifunctional membrane proteins linked to best disease and other retinopathies. Physiol. Rev. *88*, 639-672.

Jentsch, T.J., Stein, V., Weinreich, F., and Zdebik, A.A. (2002). Molecular structure and physiological function of chloride channels. Physiol. Rev. 82, 503-568.

Jo, S., Yarishkin, O., Hwang, Y.J., Chun, Y.E., Park, M., Woo, D.H., Bae, J.Y., Kim, T., Lee, J., Chun, H., et al. (2014). GABA from reactive astrocytes impairs memory in mouse models of Alzheimer's disease. Nat. Med. 20, 886-896.

Kane Dickson, V., Pedi, L., and Long, S.B. (2014). Structure and insights into the function of a Ca(2+)-activated Cl(-) channel. Nature, *516*, 213-218.

Kim, K.W., Hwang, J., Kim, D.H., Park, H., and Lim, H.H. (2023). Cytosolic domain regulates the calcium sensitivity and surface expression of BEST1 channels in the HEK293 cells. BMB Rep. *56*, 172-177.

Koh, W., Park, M., Chun, Y.E., Lee, J., Shim, H.S., Park, M.G., Kim, S., Sa, M., Joo, J., Kang, H., et al. (2022). Astrocytes render memory flexible by releasing d-serine and regulating NMDA receptor tone in the hippocampus. Biol. Psychiatry, *91*, 740-752.

Kumar, N.M., and Gilula, N.B. (1996). The gap junction communication channel. Cell, *84*, 381-388.

Lee, S., Yoon, B.E., Berglund, K., Oh, S.J., Park, H., Shin, H.S., Augustine, G.J., and Lee, C.J. (2010). Channel-mediated tonic GABA release from glia. Science, *330*, 790-796.

Marmorstein, A.D., Marmorstein, L.Y., Rayborn, M., Wang, X., Hollyfield, J.G., and Petrukhin, K. (2000). Bestrophin, the product of the Best vitelliform macular dystrophy gene (VMD2), localizes to the basolateral plasma membrane of the retinal pigment epithelium. Proc. Natl. Acad. Sci. U.S.A. 97, 12758-12763.

- Milenkovic, V.M., Langmann, T., Schreiber, R., Kunzelmann, K., and Weber, B.H. (2008). Molecular evolution and functional divergence of the bestrophin protein family. BMC Evol. Biol. 8, 72.
- Miller, A.N., Vaisey, G., and Long, S.B. (2019). Molecular mechanisms of gating in the calcium-activated chloride channel bestrophin. Elife, 8, Article e43231.
- O'Driscoll, K.E., Leblanc, N., Hatton, W.J., and Britton, F.C. (2009). Functional properties of murine bestrophin 1 channel. Biochem. Biophys. Res. Commun. 384, 476-481.
- Oh, S.J., Han, K.S., Park, H., Woo, D.H., Kim, H.Y., Traynelis, S.F., and Lee, C.J. (2012). Protease activated receptor 1-induced glutamate release in cultured astrocytes is mediated by Bestrophin-1 channel but not by vesicular exocytosis. Mol. Brain, 5, 38.
- Oh, S.J., and Lee, C.J. (2017). Distribution and function of the bestrophin-1 (Best1) channel in the brain. Exp. Neurobiol. 26, 113-121.
- Owji, A.P., Kittredge, A., Zhang, Y., and Yang, T. (2021). Structure and function of the bestrophin family of calcium-activated chloride channels. Channels (Austin), 15, 604-623.
- Owji, A.P., Wang, J., Kittredge, A., Clark, Z., Zhang, Y., Hendrickson, W.A., and Yang, T. (2022a). Structures and gating mechanisms of human bestrophin anion channels. Nat. Commun. 13, 3836.
- Owji, A.P., Yu, K., Kittredge, A., Wang, J., Zhang, Y., and Yang, T. (2022b). Bestrophin-2 and glutamine synthetase form a complex for glutamate release. Nature, 611, 180-187.
- Owji, A.P., Zhao, Q., Ji, C., Kittredge, A., Hopiavuori, A., Fu, Z., Ward, N., Clarke, O.B., Shen, Y., Zhang, Y., et al. (2020). Structural and functional characterization of the bestrophin-2 anion channel. Nat. Struct. Mol. Biol. 27, 382-391.
- Pant, S., Tam, S.W., and Long, S.B. (2024). The pentameric chloride channel BEST1 is activated by extracellular GABA. bioRxiv 11.22.624909.
- Park, H., Han, K.S., Seo, J., Lee, J., Dravid, S.M., Woo, J., Chun, H., Cho, S., Bae, J.Y., An, H., et al. (2015). Channel-mediated astrocytic glutamate modulates hippocampal synaptic plasticity by activating postsynaptic NMDA receptors. Mol. Brain, 8, 7.
- Park, H., Oh, S.J., Han, K.S., Woo, D.H., Park, H., Mannaioni, G., Traynelis, S.F., and Lee, C.J. (2009). Bestrophin-1 encodes for the Ca2+-activated anion channel in hippocampal astrocytes. J. Neurosci. 29, 13063-13073.
- Park, K., Lee, B.C., and Lim, H.H. (2019). Mutation of external glutamate residue reveals a new intermediate transport state and anion binding site in a CLC CI(-)/H(+) antiporter. Proc. Natl. Acad. Sci. U.S.A. 116, 17345-17354.
- Ponjavic, V., Eksandh, L., Andreasson, S., Sjostrom, K., Bakall, B., Ingvast, S., Wadelius, C., and Ehinger, B. (1999). Clinical expression of

- Best's vitelliform macular dystrophy in Swedish families with mutations in the bestrophin gene. Ophthalmic Genet. 20, 251-257.
- Punjani, A., Rubinstein, J.L., Fleet, D.J., and Brubaker, M.A. (2017). cryoSPARC: algorithms for rapid unsupervised cryo-EM structure determination. Nat. Methods, 14, 290-296.
- Punjani, A., Zhang, H., and Fleet, D.J. (2020). Non-uniform refinement: adaptive regularization improves single-particle cryo-EM reconstruction. Nat. Methods, 17, 1214-1221.
- Qu, Z., Cui, Y., and Hartzell, C. (2006). A short motif in the C-terminus of mouse bestrophin 3 [corrected] inhibits its activation as a CI channel. FEBS Lett. 580, 2141-2146.
- Qu, Z.Q., Yu, K., Cui, Y.Y., Ying, C., and Hartzell, C. (2007). Activation of bestrophin CI- channels is regulated by C-terminal domains. J. Biol. Chem. 282, 17460-17467.
- Roh, J.W., Choi, H.W., and Gee, H.Y. (2025). Guidelines for plasma membrane protein detection by surface biotinylation. Mol. Cells, 48, Article 100174.
- Smart, O.S., Neduvelil, J.G., Wang, X., Wallace, B.A., and Sansom, M.S. (1996). HOLE: a program for the analysis of the pore dimensions of ion channel structural models. J. Mol. Graph. 14, 354-360.
- Sun, H., Tsunenari, T., Yau, K.W., and Nathans, J. (2002). The vitelliform macular dystrophy protein defines a new family of chloride channels. Proc. Natl. Acad. Sci. U.S.A. 99, 4008-4013.
- Tsunenari, T., Sun, H., Williams, J., Cahill, H., Smallwood, P., Yau, K.W., and Nathans, J. (2003). Structure-function analysis of the bestrophin family of anion channels. J. Biol. Chem. 278, 41114-41125.
- Vaisey, G., and Long, S.B. (2018). An allosteric mechanism of inactivation in the calcium-dependent chloride channel BEST1. J. Gen. Physiol. 150, 1484-1497.
- Vaisey, G., Miller, A.N., and Long, S.B. (2016). Distinct regions that control ion selectivity and calcium-dependent activation in the bestrophin ion channel. Proc. Natl. Acad. Sci. U.S.A. 113, E7399-E7408.
- Wang, J., Owji, A.P., Kittredge, A., Clark, Z., Zhang, Y., and Yang, T. (2024). GAD65 tunes the functions of Best1 as a GABA receptor and a neurotransmitter conducting channel. Nat. Commun. 15, 8051.
- Woo, D.H., Han, K.S., Shim, J.W., Yoon, B.E., Kim, E., Bae, J.Y., Oh, S.J., Hwang, E.M., Marmorstein, A.D., Bae, Y.C., et al. (2012). TREK-1 and Best1 channels mediate fast and slow glutamate release in astrocytes upon GPCR activation. Cell, 151, 25-40.
- Xiao, Q., Prussia, A., Yu, K., Cui, Y.Y., and Hartzell, H.C. (2008). Regulation of bestrophin CI channels by calcium: role of the C terminus. J. Gen. Physiol. 132, 681-692.